

An X-ray spectroscopic Study of the Hot Interstellar Medium Toward the Galactic Bulge

Toshishige HAGIHARA¹*, Noriko Y. YAMASAKI¹, Kazuhisa MITSUDA¹, Yoh TAKEI¹, Kazuhiro SAKAI¹, Yangsen YAO², Q. Daniel WANG³, Dan MCCAMMON⁴

yamasaki@astro.isas.jaxa.jp

¹*Institute of Space and Astronautical Science, Japan Aerospace Exploration Agency
3-1-1 Yoshinodai, Chuo, Sagami-hara, 252-5210*

²*University of Colorado, CASA, 389 UCB, Boulder, CO 80309, USA*

³*Department of Astronomy, University of Massachusetts, Amherst, MA 01003, USA*

⁴*Department of Physics, University of Wisconsin, Madison, 1150 University Avenue, Madison, WI 53706, USA*

(Received 2011 February 25; accepted 2011 August 22)

Abstract

We present a detailed spectroscopic study of the hot gas toward the Galactic bulge along the 4U 1820–303 sight line by a combination analysis of emission and absorption spectra. In addition to the absorption lines of O VII K_{α} , O VII K_{β} , O VIII K_{α} and Ne IX K_{α} by Chandra LTGS as shown by previous works, Suzaku detected clearly the emission lines of O VII, O VIII, Ne IX and Ne X from the vicinity. We used simplified plasma models with constant temperature and density. Evaluation of the background and foreground emission was performed carefully, including stellar X-ray contribution based on the recent X-ray observational results and stellar distribution simulator. If we assume that one plasma component exists in front of 4U1820–303 and the other one at the back, the obtained temperatures are $T = 1.7 \pm 0.2 \times 10^6$ K for the front-side plasma and $T = 3.9_{-0.3}^{+0.4} \times 10^6$ K for the back-side. This scheme is consistent with a hot and thick ISM disk as suggested by the extragalactic source observations and an X-ray bulge around the Galactic center.

Key words: Galaxy:bulge – X-rays:diffuse background – X-rays:ISM – X-rays:stars

1. Introduction

X-ray surveys, such as the ROSAT All Sky Survey (RASS), show that there is a large enhancement of the emission in the Galactic center region expanding to $\pm 30^\circ$ in longitude and latitude, which is called an X-ray bulge. Snowden et al. (1997) summed 3/4 keV (0.4 – 1.2 keV) and 1.5 keV (0.7–2.0 keV) RASS data with 10° wide bins centered on $\ell = 353^\circ$ and checked the latitude profile of the surface brightness. They found that the intensity distribution of the enhancement in the $b > 0^\circ$ region and the $b < 0^\circ$ region significantly differed. They construct an isothermal ($T = 10^{6.6}$ K) cylinder plasma model with an exponential fall-off in density with height above the plane and showed that the enhancement for $b < 0^\circ$ can be well explained by this model. The hot gas cylinder is located at the galactic center and its required radius is 5.6 kpc, with an electron density of $3.5 \times 10^{-3} \text{ cm}^{-3}$ in the disk and a scale height of 1.9 kpc. They also suggest that in the $b > 0^\circ$ region, this model always produces less intensity than the data and this implies an additional component, such as Loop I. The total luminosity of the plasma cylinder was $1.9 \times 10^{39} \text{ erg s}^{-1}$ and the mass was $\sim 3 \times 10^7 M_{\odot}$. A molecular cloud of $\sim 10^{21} \text{ cm}^{-2}$ hydrogen column density is opaque to soft X-rays lower than 0.5 keV. Shadowing observa-

tions using such molecular clouds located a few kpc away provide important clues. Park et al. (1997) observed the $(\ell, b) = (-10^\circ, 0^\circ)$ direction with ROSAT, where a molecular cloud is located ~ 3 kpc away, and showed an anti-correlation of the molecular cloud density and X-ray intensity. They compare the X-ray intensity in on-cloud and off-cloud directions to find that almost 40% of the emission in both the 3/4 and 1.5 keV band comes from behind the cloud. Almy et al. (2000) also carried out a shadowing analysis using ROSAT PSPC data for $(\ell, b) \sim (337^\circ, 4^\circ)$, with an absorption column density assumed from IR (100 μm) intensity, and revealed that more than 70 % of the emission is due to X-ray sources behind the cloud.

Recent studies reveal that there are many kinds of X-ray emitters in our Galaxy. Not only the hot ISM in the Galactic disk and halo (Yao et al. 2009; Hagihara et al. 2010; Yoshino et al. 2009), but also CVs and normal stars can contribute to the unresolved emission in the Galaxy (Masui et al. 2009). In order to distinguish between the diffuse plasma emission and the sum of faint point sources, measurements of the absorption line due to the plasma is essential, and combination study of the absorption and emission spectra can solve the density and scale of the plasma, as shown by the observation of the hot halo around our Galaxy using extragalactic objects as background sources (Yao et al. 2009; Hagihara et al. 2010).

Absorption observations toward the X-ray bulge were

* Present Address is Cybozu Inc., 1-4-14 Kouraku, Bunkyo, Tokyo 112-0004

carried out with an X-ray grating detector. The X-ray binary 4U 1820–303 is located in the globular cluster NGC 6624 at $(\ell, b) \sim (2.8^\circ, -7.9^\circ)$, 7.6 ± 0.4 kpc away (Kuulkers et al. 2003) as illustrated in figure 1. It was observed with the high resolution grating onboard Chandra and absorption lines of O VII, O VIII and Ne VIII were reported (Futamoto et al. 2004; Yao & Wang 2006). Futamoto et al. (2004) analyzed data using curve of growth and constrained the column density of each ion as $\log N_{\text{OVII}} = 16.2 - 16.7$, $\log N_{\text{OVIII}} = 15.9 - 16.5$ and $\log N_{\text{NeIX}} = 15.7 - 16.1$. The velocity dispersion (v_b) was derived using joint analysis of O VII K α and O VII K β to $v_b > 200$ km s $^{-1}$, and the column density of O VIII and Ne IX are derived assuming the same velocity dispersion constraint as O VII. Meanwhile Yao & Wang (2006) used their absline absorption model on the same data and reported the column density as $\log N_{\text{OVII}} = 16.3 \pm 0.2$, $\log N_{\text{OVIII}} = 16.4 \pm 0.2$ and $\log N_{\text{NeIX}} = 16.0 \pm 0.1$ and the velocity dispersion was 255_{-90}^{+114} km s $^{-1}$.

In this paper, we will use an emission spectrum obtained by Suzaku for a region $\sim 2^\circ$ away from 4U1820–303. A combined analysis using the same method as used in the Galactic halo study with extragalactic objects by Yao et al. (2009) and Hagihara et al. (2010), in consideration with foreground diffuse and discrete emission will give us further information about the density and scale of the hot gas in the Galactic bulge region.

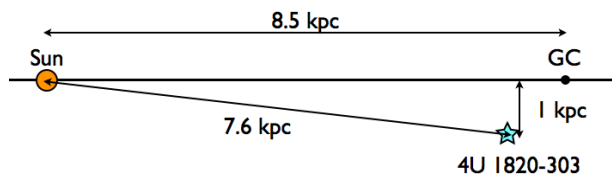


Fig. 1. Geometry of the sight line toward 4U 1820–303 and the Galactic plane

2. Observation and Data Reduction

The observation logs of the Chandra and Suzaku data are summarized in table 1. 4U1820–303 was observed three times by Chandra, but we used only the HRC-S + LETG data to obtain the best energy resolution. The dataset and data reduction process is basically the same as in Yao & Wang (2006), but we followed the procedure presented in Yao et al. (2009) to extract the first order spectra of the LETG.

Our Suzaku observations were taken with the CCD camera X-ray Imaging Spectrometer (XIS; Koyama et al. 2007, Mitsuda et al. 2007). The XIS was set to the normal clocking mode and the spaced-raw charge injection (SCI) was applied to the data during the observations. We used processing data version 2.2.7.18 for the two observations. In this work, we used only the spectrum obtained with XIS1.

We adopted the same data screening as in Hagihara et al. (2010), i.e., standard data screening in addition to

the exclusion of the thick atmospheric neutral oxygen column density in the line of sight (Smith et al. 2007) and of the Solar wind charge exchange (SWCX) (Fujimoto et al. 2007). We found that the counting rate was constant as a function of the neutral oxygen column density for the cleaned data. Thus, there is no significant neutral oxygen emission from the Earth’s atmosphere in the filtered data. The solar wind intensity obtained with the Solar Wind Electron Proton and Alpha Monitor (SWEPAM) aboard the *Advanced Composition Explorer* (ACE) was checked. We removed the time intervals when the proton flux in the solar wind exceeded 4×10^8 cm $^{-2}$ s $^{-1}$ (Masui et al. 2009). With this criterion, we discarded 19.7 ksec of the exposure and the net exposure time became 32.2 ksec.

There are no obvious discrete X-ray sources in the X-ray images for the 0.4–1.0 keV energy range. However, there would be many low luminosity sources in this direction, thus we applied a wavelet analysis using CIAO: wvdetect, to detect such point sources. We found 23 point source candidates in the fields and removed a circular region with 1’ radius centered at the source position from the data. These candidates can be caused by statistical fluctuations, and so we have to check them. We then compared the spectrum including the possible point sources and the spectrum excluding them and found there is no significant difference. To increase the photon counts and reduce the statistical error, we decided to use data including the point source candidates in further analysis.

We constructed instrumental response files (rmfs) and effective area files (arf) by running the scripts *xisrmfgen* and *xissimarfgen* (Ishisaki et al. 2007). To take into account the stray light coming from outside of the CCD fov, we used a 20’ radius flat field as the input emission in calculating the arf. We also included in the arf file the degradation of low energy efficiency due to the contamination on the XIS optical blocking filter. The versions of calibration files used here were *ae_xi1_quanteff_20080504.fits*, *ae_xi1_rmffparam_20080901.fits*, *ae_xi1_makepi_20080825.fits* and *ae_xi1_contami_20071224.fits*. We estimated the non-X-ray-background from the night Earth database using the method described in Tawa et al. (2008).

3. Analysis and Results

3.1. Absorption spectrum analysis

We first calculated the equivalent widths (EWs). We constructed a model with a power-law and narrow Gaussians and fitted the spectra in narrow ranges as shown in table 2, and obtained EWs for each line using the eqwidth tool in Xspec. The errors in the equivalent widths are obtained as following; 1) we calculated the 90% error range of the normalization of the gaussian function. 2) Next, we calculated the maximum error of the EW (EW_{max}) using normalization values of the best fit (N_{best}) and maximum (N_{max}) as $EW_{\text{max}} = EW/N_{\text{best}} \times N_{\text{max}}$. Comparing the previous work, our obtained value for the O VII K α

Table 1. Observation logs

Target name	(ℓ, b)	ID	Instrument	Obs.Start date	Exposure (ksec)
4U1820-30	(2.8°, -7.9°)	98	Chandra HRC-S+LETG	2000-03-10	15.1
Bulge 3	(1.3°, -7.5°)	500001010	Suzaku XIS	2006-03-06	51.9 (32.2) [†]

[†] Value in parenthesis is the exposure time after data screening (see text)

Table 2. Equivalent widths of absorption lines in 4U1820-303 spectrum

	O VII $K\alpha$	O VIII $K\alpha$	O VII $K\beta$	Ne IX $K\alpha$	Ne X $K\alpha$
Centroid (keV)	0.5734	0.6537	0.6663	0.9223	1.022
EW (eV)	0.65 ^{+0.19} _{-0.14}	0.69 ^{+0.17} _{-0.20}	0.19 ^{+0.16} _{-0.16}	0.52 ^{+0.24} _{-0.22}	< 0.16
EW (mÅ)	24.4 ^{+7.1} _{-5.2}	19.9 ^{+4.9} _{-5.8}	5.3 ^{+4.4} _{-4.4}	7.5 ^{+3.4} _{-3.2}	< 1.9
Fitting Range(Å)	20-22	18-20	18-20	12-14	11.4-12.5

(0.65^{+0.19}_{-0.14} eV) is smaller than those in Futamoto et al. (2004) (1.19^{+0.47}_{-0.30} eV) and Yao & Wang (2006) (1.06^{+0.34}_{-0.27} eV). We confirmed that this difference comes from the modeling of the continuum spectrum, with higher order diffraction photons (Yao & Wang 2006). We used only the 1st order spectrum of the HRC observation, and modeled the continuum spectrum in a narrow energy range, to obtain reliable values.

To obtain the column density of ions and to estimate the total column density of the absorbing material, we fit all the lines simultaneously. We first fitted the continuum between 0.54 and 1.1 keV with a continuum model of a blackbody and a broken power-law. Foreground absorption by the neutral ISM with solar metal abundances by Anders & Grevesse (1989) is assumed. This model returned a minimum $\chi^2/\text{dof} = 858.1/577$ and the best-fit column density of the neutral ISM N_{H} is $1.9 \times 10^{21} \text{cm}^{-2}$. This value is consistent with N_{H} estimated from by the 100 μm intensity ($2.3 \times 10^{21} \text{cm}^{-2}$) and reported in Yao & Wang (2006).

This poor fit might be caused by residuals at the metal edge due to uncertainties in the Chandra response matrices. Nicastro et al. (2005) set the metal abundance of the neutral absorption material to be free to deal with this problem. As we followed their method, it decreases the residuals ($\chi^2/\text{dof} = 761.1/560$) with the virtual absence of Ne and Na, and an over-abundance of C, N and Mg by factors of 3, 3 and 26 respectively. These values are due to the uncertainties in calibration, rather than true ISM metallicity (Nicastro et al. 2005). Though the χ^2 is still not good, it is difficult to compensate the calibration uncertainties further and we use this model to describe the continuum.

We next added two absorption lines representing O VII $K\alpha$ and O VII $K\beta$ using the absem model, which is the same as in Hagihara et al. (2010). The column density and velocity dispersion of these lines are linked because both lines originate from the same ionization state of oxygen (model A1). The results are given in table 3. We next added absorption lines representing O VIII $K\alpha$ and Ne IX $K\alpha$ step by step (model A2, A3). In each step, the velocity dispersion of lines are linked together. The results

maintain consistency, thus in further analysis the velocity dispersion is always linked together. For the next step, we evaluated the hot phase hydrogen column density assuming solar abundances of O and Ne (model A4) (see figure 2). We then let the Ne abundance vary and fitted the spectrum (model A4'). Please note that we fixed the abundance of O to the solar value, because the contribution of continuum emission is small and it is hard to determine the absolute metallicity. Though the best fit hydrogen column density become smaller and the Ne abundance is $2.2^{+1.8}_{-1.3}$, all the parameters are consistent with those of the A4 model. We will use this A4 model for further combined analysis, and evaluate the Ne/O abundance effects if necessary. There might be intrinsic absorbing material around the 4U1820-303. Futamoto et al. (2004) discuss the possibility of intrinsic absorption using a photo-ionization simulator and conclude that the size of the binary system and the luminosity cannot explain the O VII ionization fraction estimated by the column density ratio. Thus we consider that all of these absorption lines originate in the hot ISM in the further analysis.

3.2. Emission spectrum analysis

3.2.1. Modeling of the contribution from foreground emission and stars

The emission spectrum from the 4U1820-303 vicinity obtained by Suzaku is shown in figure 3. The emission below 2 keV is very bright, and we can easily distinguish the emission lines of O VII, O VIII, Ne IX, and Ne X. We evaluated the intensity of these lines by a simple power-law and Gaussians fitting model (model E1) and the results are summarized in table 4. Hereafter, the intensity of the line emission is shown in LU (Line Units), which corresponds to photons $\text{s}^{-1} \text{cm}^{-2} \text{str}^{-1}$. These line ratios are hard to reproduce with a single -temperature plasma. Thus we will study several components that can contribute to the emission in this region. We will consider the diffuse emission from the Solar neighborhood, Loop I, and contribution from stars in the Galaxy, step by step.

As shown by the Suzaku shadowing observations of MBM-12 molecular clouds (Smith et al. 2007) and the evaluation of the soft X-ray background spectra of 14 fields

Table 3. Parameters of the hot ISM absorbing the 4U1820–303 spectrum

Model	v_b (km s ⁻¹)	log N (cm ⁻²)				Abundance Ne/O	log T (K) T_1	χ^2/dof
		O VII	O VIII	Ne IX	H _{HOT}			
A1	163 ⁺²¹⁹ ₋₇₇	16.17 ^{+0.33} _{-0.21}	708.4/573
A2	239 ⁺³⁰¹ ₋₁₀₂	16.10 ^{+0.37} _{-0.16}	15.90 ^{+0.37} _{-0.17}	671.2/571
A3	191 ⁺²⁵⁴ ₋₁₀₁	16.14 ^{+0.35} _{-0.19}	15.92 ^{+0.42} _{-0.19}	15.87 ^{+0.30} _{-0.33}	759.9/569
A4	112 ⁺¹¹⁴ ₋₂₆	19.66 ^{+0.16} _{-0.16}	...	6.27 ^{+0.13} _{-0.07}	662.1/570
A4'	187 ⁺²⁵⁴ ₋₉₈	19.46 ^{+0.34} _{-0.15}	2.2 ^{+1.8} _{-1.3}	6.28 ^{+0.06} _{-0.06}	659.8/569

Table 4. Apparent surface brightness of each line. (model E1)

O VII (LU)	O VIII (LU)	Ne IX (LU)	Ne X (LU)
23.45 ^{+3.21} _{-1.71}	18.96 ^{+0.87} _{-2.25}	10.49 ^{+0.49} _{-1.22}	5.99 ^{+0.76} _{-0.58}

(Yoshino et al. 2009), emission around our Solar neighborhood due to Solar wind charge exchange and/or the Local hot bubble is present. Most of the emission from the Solar neighborhood might be below 0.5 keV, except for ~ 2 LU of O VII emission line. The apparent spectrum above 0.5 keV can be reproduced by an optically thin thermal plasma emission in collisional ionization equilibrium (CIE) with $kT \sim 0.1$ keV (Yoshino et al. 2009). As the uncertainty of the O VII line intensity is ~ 1 LU, we adopt these values as the foreground emission.

The sight line toward 4U 1820–303 would go through the Loop I, a large structure seen in the radio waveband. This structure is considered to be an old SNR (10^6 years) located in Sco-Cen OB association. Egger & Aschenbach (1995) modeled this SNR based on RASS data. The density and temperature in the cavity are 2.5×10^{-3} cm⁻³ and 4.6×10^6 K. We then assumed the column density and line intensity using these parameters as shown in table 5. After comparing these values with those in table 3 and 4, we will neglect the effect of Loop-I in the absorption line analysis, but take it into account in the emission line analysis.

Recently, the contribution of stars in the soft X-ray background was studied using Chandra, XMM-Newton (López-Santiago et al. 2007) and Suzaku (Masui et al. 2009). The typical luminosity of a stellar corona is as small as 10^{29} erg s⁻¹, but the number density is large in the Galactic plane and bulge direction. We estimated the contribution from stars by the following steps. First, we estimated the number of stars in the field-of-view, using a stellar population model. Secondly, we calculated the X-ray flux and spectra based on the currently available observational properties.

We used TRILEGAL simulator ver 1.4¹ (Girardi et al. 2005) to estimate the main sequence stellar distribution in the observing cone. This simulator synthesizes a stellar population for a given Galaxy field. Vanhollebeke

et al. (2009) used this simulator and compared the results with Two Micron All Sky Survey (2MASS) (Skrutskie et al. 2006) and Optical Gravitational Lensing Experiment (OGLE) (Udalski et al. 1997) observational data in 11 directions. There is a discrepancy of about 20% between the model and data, especially in the number of low luminosity stars. We used their best model parameters, to create the mock population, and counted the stars of several spectral types, and ages as shown in table 6. Clearly, there are lots of A, F, G, K, and M stars in the Suzaku field of view. Note that we count the stars in a radius of $20'$ in the Suzaku sight line, and estimated the observed flux on the detector via the arf. Kuntz & Snowden (2001) estimated the X-ray luminosity of these stars based on the ROSAT data, and Rocks (2009) compiled the X-ray spectra after López-Santiago et al. (2007) which uses XMM-Newton observation. We used the values shown in table 7 as a template of each spectral type stars. In López-Santiago et al. (2007), about half of the K and M stars are represented by the two-temperature coronal model, and the other half is described by a single-temperature coronal model. We added the flux from the mock star distribution with these X-ray luminosity and spectra, by 8 thin thermal plasmas as an empirical mock-up spectrum. The RS CVn type binaries are also bright in X-rays, with a typical X-ray luminosity $> 10^{30}$ erg s⁻¹. We adopt a simple exponential disk model by Ottmann & Schmitt (1992), and found that the estimated numbers in a circle of $20'$ is about ~ 980 .

The HI column density toward the observing direction by 21 cm radio observation is 1.36×10^{21} cm⁻² (Kalberla et al. 2005). The HI +H₂ column derived by IRAS 100 μ m intensity with a conversion formula by Snowden et al. (1993) is 1.42×10^{21} cm⁻². We also calculated the hydrogen column as a function of the distance from the Sun based on the global Galactic model by Ferriere (1998), and found that $\sim 80\%$ of the absorption material is located within 2 kpc from us. Thus, as a crude assumption, we do not apply absorption by the neutral ISM to the SWCX+LHB component, Loop I, and stars and RS CVns within 2 kpc, but we do apply the absorption of 1.42×10^{21} cm⁻² for stars and RS CVns beyond 2 kpc.

3.2.2. Hot ISM emission

We then try to represent the observed energy spectrum with contributions from stars and RS CVns and the Cosmic X-ray Background (CXB), which is modeled as

¹ <http://stev.oapd.inaf.it/cgi-bin/trilegal>

Table 5. Estimated contribution from the Solar neighborhood and Loop I

Model	Line Intensity (LU)				Column Density ($\log N/(\text{cm}^{-2})$)			
	O VII	O VIII	Ne IX	Ne X	O VII	O VIII	Ne IX	Ne X
Solar neighborhood	2	0	0	0
Loop I	1.83	2.10	0.31	0.04	14.3	14.8	14.3	13.8

Table 6. Criteria and number of stars in the direction of Suzaku observation within a radius of 20' for each spectral type

spectral type	(B-V) ₀	M_V	0-0.15 Gyr	0.15-1 Gyr	1-10 Gyr	>10 Gyr
O+B	<-0.01	...	8	6	7	0
A	-0.01-0.3	...	6	58	12	90
F	0.3-0.6	2-8	12	78	35212	41152
G	0.6-0.8	2-10	6	58	97672	29270
K	>0.8	<8	41	240	454739	72546
M(early)	>0.8	8-15	133	1054	1851091	407848
M(late)	>0.8	>15	0	0	35	0

an absorbed power-law with a photon index of 1.4 and its normalization of about $10 \text{ photon sec}^{-1} \text{ cm}^{-2} \text{ str}^{-1} \text{ keV}^{-1}$ at 1 keV (Hasinger et al. 1993). This model only reproduces about 1/10 of the emission below 1 keV. Even though we allowed the normalization of every stellar component to vary, it was impossible to exhibit enough O VII line because the temperature of the stellar components are all high.

We next added a hot ISM component to reproduce the spectrum. We tried a one temperature hot ISM model with fixed and free (N, Ne and Fe) abundance and obtained poor χ^2/dof value of 578.62/133 and 366.20/130 respectively. This poor fit is caused by the spectrum where O VII and Ne X lines both exist and it is difficult for a single temperature plasma to reproduce these lines simultaneously. We then gave up the one temperature hot ISM model and tried a two temperature model with fixed abundance (model E1). Though the χ^2 was improved to 358.17/131, there are still significant residuals between the model and spectrum as shown in figure 4. It is obvious that a continuum-like component is needed to reduce the residuals between 1 and 3 keV, thus we tried to free the CXB parameters. Though this model reduced the residuals and improved the χ^2/dof to 121.85/129, the best fit values of photon index is $2.4_{-0.1}^{+0.1}$ and the normalization is $41.5_{-7.6}^{+3.6} \text{ photon sec}^{-1} \text{ cm}^{-2} \text{ str}^{-1} \text{ keV}^{-1}$ at 1 keV. The flux is about 4 times larger than the nominal value (Hasinger et al. 1993) and is not reasonable for the CXB even though its fluctuation is taken into account.

As mentioned before, there are large uncertainties in the number densities, luminosities, and the energy spectrum of the background low luminosity stars and binaries. For this reason, we tried the following two models.

- Model E2: Assuming an underestimation of the stellar contribution, the normalization of the background stars and RS CVns are set to be free.
- Model E3: Assuming an unknown thermal compo-

nent in the bulge, one high temperature thin thermal plasma emission model is added.

In the E2 model, we set the normalization of stars to be free step by step and investigated the residuals and the normalization and estimated the effect of star contributions on the hot ISM properties. To compensate for the residuals around 2 keV, we needed an additional $\sim 2\text{keV}$ component. One plausible component to produce such hard emission is RS CVn binaries of which we modeled a spectrum with a two temperature plasma of 2.59 keV and 0.17 keV. Moreover it is not well understood how many stars make binaries and there is uncertainty in the distribution of the RS CVn binaries. Thus we first set the normalization of background binary components to be free (Model E2-b: The emission model with background binary normalization is set to be free). Though we found that this model certainly reduced the residuals around 2 keV, we also found that this model caused significant residuals around 1 keV and above 2.5 keV. Emission from plasma of $kT = 2.59 \text{ keV}$ is a little too high to compensate for the residual.

The M type stars exhibit coronal emission whose temperature is empirically known to be $kT = 0.5 \sim 1.2 \text{ keV}$, and characterized by complex emission with Ne, and Fe-L lines around 0.9 keV, (López-Santiago et al. 2007; Sciortino et al. 1999) and their low luminosity could cause large uncertainties in the number of stars within the FOV. For the next step, we fixed the binary normalization to the simulated value and set the normalization of the M type star to be free (Model E2-m: Emission model with background M type star normalization is set to be free). This model also could not explain the entire spectrum. However, residuals caused by these two models (E2-b and E2-m) are complementary.

We thus tried to free the normalization of binary and M stars simultaneously (model E2-mb). This model fit the data with χ^2/dof of 144.37/131. The normalization ratios

Table 7. Stellar type parameters used in stellar emission estimation. The empirical spectral model are summarized by Rocks (2009) after López-Santiago et al. (2007) and luminosities estimated by Kuntz & Snowden (2001). RS-CVn type binary parameters after Ottmann & Schmitt (1992) are also shown.

Spectral type	Single temperature	Two temperature model			Abundance		$\log L_X (\text{erg s}^{-1})^\dagger$		
	kT (keV)	kT_{hot} (keV)	kT_{cool} (keV)	$EM_{\text{cool}}/EM_{\text{hot}}$	Z_\odot	0–0.15 Gyr	Age		
							0.15–1 Gyr	1–10 Gyr	
F	0.58	0.5	29.51	29.02	28.13	
G	0.67	0.3	29.91	28.82	27.89	
K	0.83	1.17	0.32	1.97	0.2	29.66	28.52	27.89	
M(early)	0.90	0.80	0.27	2.02	0.1	29.31	28.49	27.54	
RS-CVn	N/A	2.59	0.17	0.22	1.0		30.75 ‡		

† Luminosity in 0.1–2.4 keV

‡ Luminosity in 0.4–4.0 keV independent of age

to the simulated values are $6.57^{+1.17}_{-2.14}$ and $5.45^{+1.27}_{-2.20}$ for M stars and binaries respectively. It is difficult to confirm if these values are correct or not, so we accept this value at present.

We then set the normalization of the K type star and F and G type star to be free sequentially (model E2-mkb, E2-mkfgb). This modification caused no significant changes to the fitting results and the contribution of K, F and G stars vanished. Finally we linked the normalization of all star components and set them to be free (model E2-(mkgf)b). The ratios of the obtained normalization to the simulated values are $2.79^{+0.74}_{-0.78}$ and $6.22^{+1.35}_{-1.35}$ for all spectral type stars and binaries respectively. χ^2/dof is 151.29/129 and it is hard to explain the whole spectra with this model.

The normalizations and temperatures of the cooler and hotter hot ISM are consistent with each other in the three models (E2-mb, E2-mkb, E2-mkfgb). From these results, the normalization of the stars is of little effect on the hot ISM temperature.

In the E3 model, an additional unknown component is assumed. We therefore fixed all the components to the simulated values, other than the hot ISM. First, we added a thin thermal plasma to the model because the contribution from an unknown stellar component would be highly possible (model E3). The abundance of the additional plasma is fixed to the solar value. However this model caused residual features like the E2-b model and could not fit the data ($\chi^2/\text{dof}=165.37/131$). The metal abundance of the stellar corona is not well understood and so we set the metal abundance to be free (model E3-A). This model explain the whole spectrum very well ($\chi^2/\text{dof}=121.04/130$). However, the best fit abundance is ~ 0 and the additional component is quite close to thermal bremsstrahlung of $kT=1.1$ keV. Actually we substituted thermal bremsstrahlung for the thin thermal plasma of E3-A model and found no changes in the fitting results (model E3-B). We then set the abundance of the plasma of E3-A model to 0.1 Solar value (E3-A †). This model also fit the data with $\chi^2/\text{dof}=133.34/131$.

Some 1.5 keV thermal components are reported in the spectra of nearby dM stars (e.g. van den Besselaar et al. (2003)) and this could be the origin of the unknown component. As shown in table 7, the metallicity of the coro-

Table 10. Surface brightness of the O and Ne lines.

Model	O VII (LU)	O VIII (LU)	Ne IX (LU)	Ne X (LU)
E2-mb	$14.72^{+2.74}_{-1.47}$	$9.80^{+-0.22}_{-3.15}$	$0.61^{+1.29}_{-0.47}$	< 0.19
E3-A †	$15.80^{+2.73}_{-1.51}$	$10.75^{+1.48}_{-1.32}$	$3.09^{+1.05}_{-0.54}$	$2.17^{+1.05}_{-1.24}$

nal spectra of the low luminosity stars is very low and this is consistent with the low metallicity of the unknown component. Stellar flares are another possibility for the unknown component. In the flare period, the high temperature ($> 1\text{keV}$) component of the stellar corona become brighter than usual. It is not plausible that this unknown component originates from the hot ISM because the metallicity of the unknown component is not high ($< \sim 0.1$) and the temperature and induced pressure is too high to maintain such plasma.

From model E2 and model E3, we see that ~ 5 times normalization of stellar components or another thermal bremsstrahlung or a low abundance thin thermal plasma is needed to explain the whole spectrum. As shown in table 8 and 9, there is at most a 10% difference in hot ISM parameters between acceptable models. Our model assumes two extreme possibilities and it is reasonable to consider that the star contribution would change the hot ISM parameters at most by 10% in any case. Thus we use model E2-mb and E3-A † to represent the emission model in the further analysis.

We evaluated the line intensities corresponding to the hot ISM component with model E2-mb and E3-A † as summarized in table 10. The intensity and ratio of the O lines are little affected by the stellar or additional background models, but the contribution of the Ne lines changes by the assumption of stellar components, especially of the high temperature stars.

3.3. Combined analysis

Two thermal components are at least required to describe the emission spectrum. Assuming the geometry of the two temperature plasmas and the absorption toward the target, there are two possibilities for combined analysis. One is that only one plasma contributes the ab-

Table 8. Fitting results with model E2 (see text for details)

Model	Foreground [†]	ISM				Background [†]			χ^2/dof	
		cool		hot		Stars	RS CVn	CXB		
		$\log T$ (K) [kT (keV)]	Norm ^a	$\log T$ (K) [kT (keV)]	Norm ^a	Type ^b	Ratio ^c	Ratio ^c		
E2-b	fixed	$6.009^{+0.047}_{-0.083}$ [0.088 ^{+0.010} _{-0.015}]	$215.4^{+319.9}_{-87.6}$	$6.571^{+0.025}_{-0.022}$ [0.321 ^{+0.019} _{-0.016}]	$26.3^{+2.7}_{-2.6}$	-	fixed	$8.81^{+0.65}_{-1.28}$	fixed	167.78/132
E2-m	fixed	$6.019^{+0.067}_{-0.074}$ [0.090 ^{+0.015} _{-0.014}]	$179.6^{+212.9}_{-85.9}$	$6.524^{+0.035}_{-0.040}$ [0.288 ^{+0.024} _{-0.025}]	$18.6^{+2.9}_{-2.8}$	M	$10.61^{+1.13}_{-1.13}$	fixed	fixed	163.12/132
E2-mb	fixed	$6.012^{+0.065}_{-0.083}$ [0.089 ^{+0.014} _{-0.015}]	$195.3^{+288.8}_{-87.5}$	$6.542^{+0.036}_{-0.030}$ [0.300 ^{+0.026} _{-0.020}]	$21.5^{+3.0}_{-3.1}$	M	$6.57^{+1.17}_{-2.14}$	$5.45^{+1.27}_{-2.20}$	fixed	144.37/131
E2-mkb	fixed	$6.012^{+0.054}_{-0.080}$ [0.089 ^{+0.012} _{-0.015}]	$193.8^{+280.1}_{-84.2}$	$6.543^{+0.029}_{-0.029}$ [0.301 ^{+0.021} _{-0.020}]	$21.5^{+3.0}_{-3.0}$	M K	$7.16^{+1.71}_{-2.34}$ < 2.49	$4.93^{+1.48}_{-1.43}$	fixed	142.54/130
E2-mkgfb	fixed	$6.016^{+0.060}_{-0.082}$ [0.090 ^{+0.013} _{-0.015}]	$183.4^{+264.3}_{-82.5}$	$6.558^{+0.029}_{-0.031}$ [0.312 ^{+0.021} _{-0.021}]	$22.1^{+3.4}_{-2.8}$	M K FG	$8.21^{+1.67}_{-2.69}$ < 3.38 < 1.23	$4.60^{+1.63}_{-1.35}$	fixed	140.42/129
E2-(mkgf)b	fixed	$6.007^{+0.037}_{-0.091}$ [0.088 ^{+0.008} _{-0.016}]	$204.2^{+292.6}_{-76.2}$	$6.519^{+0.027}_{-0.030}$ [0.285 ^{+0.018} _{-0.019}]	$21.0^{+3.9}_{-3.6}$	FGKM	$2.79^{+0.74}_{-0.78}$	$6.22^{+1.35}_{-1.35}$	fixed	151.92/129
E2-mb [‡]	fixed	$6.360^{+0.020}_{-0.021}$ [0.197 ^{+0.009} _{-0.009}]	$33.7^{+3.2}_{-3.2}$	M	$11.77^{+1.11}_{-1.00}$	$2.50^{+1.43}_{-1.33}$	fixed	214.09/133
E2-mkgfb [‡]	fixed	$6.334^{+0.023}_{-0.022}$ [0.186 ^{+0.010} _{-0.009}]	$35.8^{+3.3}_{-3.4}$	M K FG	$7.01^{+2.64}_{-2.17}$ < 2.55 $4.29^{+1.31}_{-1.35}$	$4.34^{+1.52}_{-1.59}$	fixed	196.99/131

[†]All parameters are fixed to referred or simulation based value without mentioned

[‡]One hot ISM model.

^aEmission Measure $10^{-3} \int n_e n_p dl$: in unit of $\text{cm}^{-6} \text{pc}$

^bSpectral type of the stars whose normalization is set to be free

^cRatio of the normalization of stars of binaries to the simulation based value

Table 9. Fitting results of model E3

Model	Foreground [†] and backgrounds	ISM				Additional background			χ^2/dof
		cool		hot		$\log T$ (K)	Norm ^a	Abundance	
		$\log T$ (K) [kT (keV)]	Norm ^a	$\log T$ (K) [kT (keV)]	Norm ^a				
E3	fixed	$6.019^{+0.056}_{-0.062}$ [0.090 ^{+0.012} _{-0.012}]	$205.1^{+182.1}_{-87.3}$	$6.567^{+0.023}_{-0.021}$ [0.318 ^{+0.017} _{-0.015}]	$27.3^{+2.6}_{-2.6}$	$7.544^{+0.104}_{-0.082}$ [3.017 ^{+0.816} _{-0.519}]	$17.4^{+2.1}_{-2.0}$	1.0 (fixed)	165.37/131
E3-A	fixed	$6.022^{+0.078}_{-0.072}$ [0.091 ^{+0.018} _{-0.014}]	$171.0^{+190.7}_{-88.4}$	$6.546^{+0.027}_{-0.028}$ [0.303 ^{+0.020} _{-0.019}]	$24.0^{+2.8}_{-3.2}$	$7.109^{+0.105}_{-0.110}$ [1.109 ^{+0.303} _{-0.248}]	$64.3^{+27.3}_{-16.5}$	< 0.03	121.04/130
E3-B	fixed	$6.023^{+0.077}_{-0.071}$ [0.091 ^{+0.018} _{-0.014}]	$169.4^{+185.8}_{-86.9}$	$6.547^{+0.026}_{-0.025}$ [0.304 ^{+0.019} _{-0.017}]	$23.9^{+2.8}_{-2.9}$	$7.106^{+0.108}_{-0.098}$ [1.101 ^{+0.311} _{-0.222}]	$69.6^{+26.2}_{-18.4}$...	120.94/131
E3-A'	fixed	$6.017^{+0.061}_{-0.073}$ [0.090 ^{+0.013} _{-0.014}]	$193.7^{+224.9}_{-87.5}$	$6.548^{+0.026}_{-0.022}$ [0.305 ^{+0.019} _{-0.015}]	$25.9^{+2.7}_{-2.6}$	$7.239^{+0.096}_{-0.077}$ [1.495 ^{+0.372} _{-0.243}]	$38.5^{+4.8}_{-5.8}$	0.1 (fixed)	133.34/131
E3-A' [‡]	fixed	$6.440^{+0.015}_{-0.015}$ [0.237 ^{+0.008} _{-0.008}]	$37.3^{+2.3}_{-2.3}$	$7.151^{+0.038}_{-0.039}$ [1.221 ^{+0.112} _{-0.104}]	$49.8^{+4.7}_{-4.7}$	0.1	231.45/133

[†]All parameters of LHB+SWCX, Loop I, stars, and CXBs are fixed to referred or simulation based values

[‡]One hot ISM model.

^aEmission Measure $10^{-3} \int n_e n_p dl$: in unit of $\text{cm}^{-6} \text{pc}$

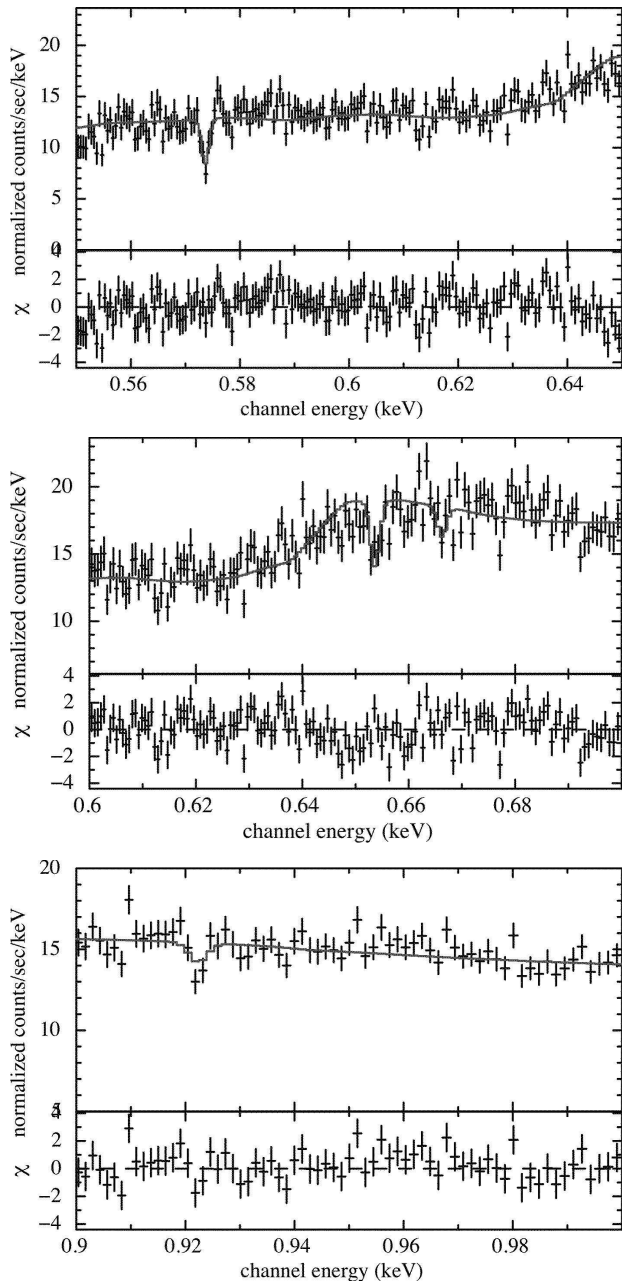


Fig. 2. O and Ne absorption lines in the 4U 1820–303 spectrum. The solid lines are model A4.

absorption, and the other is that both plasma contribute to the absorption. Thus, we consider these two cases in this section.

3.3.1. Uniform model with one absorbing plasma

We assumed first as a combined model that only one plasma contributes to the absorption (model C1). The geometry is as follows; one uniform plasma (front-side plasma) exists in front of 4U 1820–303 and another uniform plasma (back-side plasma) exists in back of 4U 1820–303, as illustrated in figure 6.

We constructed two isothermal plasma models with a uniform density, and a length L along the sight of line. We

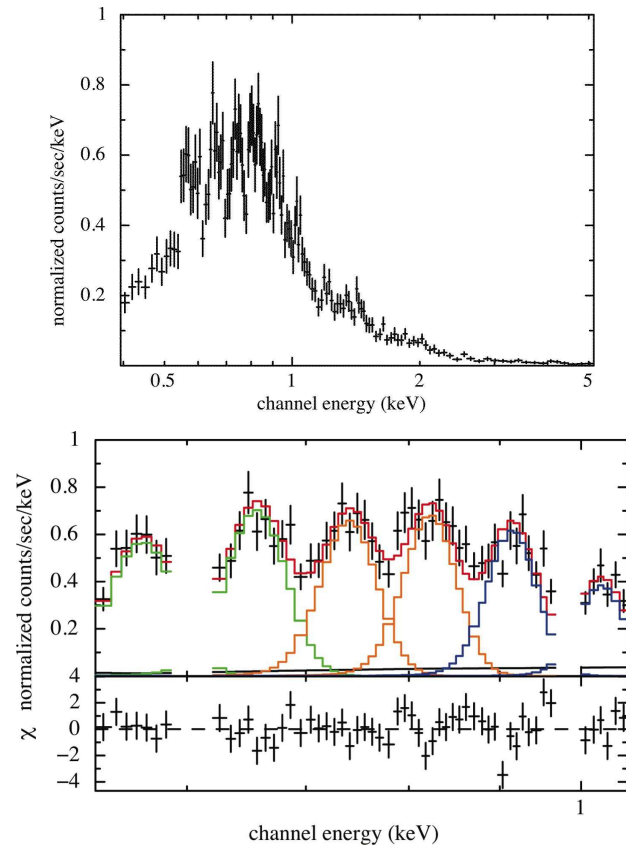


Fig. 3. Spectrum obtained in the galactic bulge region (left) and evaluation of the line intensities by Gaussians.(right)

put an upper limit of 7.6 kpc on the length of the front-side plasma, to maintain consistency with the geometry. The velocity dispersions of the plasmas are linked together because this value was mainly determined using the ratio of O VII K_α to O VII K_β in the absorption spectrum. We tried four sets of models, C1-1 and C1-2 is the combination of E2-mb and A4 model, and Ne/O abundance ratio is set to be free in C1-2. In C1-3 and C1-4 model, we adopt the E3-A' model for the emission model, and Ne/O ratio is set to be free in C1-4.

The fitting results are shown in table 11. The temperature of the front-side plasma ($T \sim 1.7 \times 10^6$ K) is determined mainly by the absorption spectra and is consistent with the temperature obtained by the absorption analysis ($T \sim 1.8 \times 10^6$ K). The temperature of the front- and back-side plasma (1.7×10^6 K and 3.9×10^6 K) are both higher than the those determined only by emission analysis (1.1×10^6 K and 3.6×10^6 K). Plasma of 1.7×10^6 K could emit O VII and O VIII lines three times and thirty times effectively than a plasma of 1.1×10^6 K. Though this makes the emission measure of the front-side plasma smaller to maintain the intensity of the O VII lines, O VIII lines are produced more effectively. Thus to suppress the O VIII intensity, the temperature of the back-side plasma becomes higher. Residuals caused by this adaptation could be compensated by the background components and this model also can reproduce the O, Fe and Ne emission

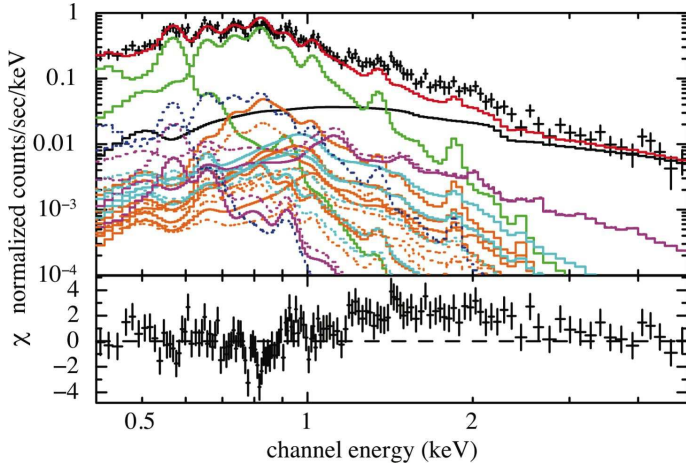


Fig. 4. Spectrum and model (E1). The dotted lines indicate foreground (unabsorbed) components and the solid lines indicate background (fully absorbed) components. hot ISM (green), CXB (black), SWCX+LHB, and Loop I (blue), stars except for M stars (orange), M stars (light blue), and RS CVns (magenta).

lines. However in the energy range lower than 0.5 keV, there are residuals caused by the deficit of N lines, because the lower temperature plasma (1.7×10^6 K) is too hot to emit N lines effectively.

We summarized the physical properties of the plasma in table 12. We assume 1, 2 and 10 kpc for the length for the back-side plasma to estimate its density and pressure, because the back-side plasma contributes to the emission, and we cannot determine the length and density separately. There could be two schemes. Assuming the back-side plasma confined in the Galactic bulge region, its length is at most 2 kpc and this leads to dense and high pressure plasma. Thus, this leads to a picture of that a hotter dense plasma existing around the Galactic center region and a warm thin plasma covering the disk. The other is that assuming pressure equilibrium between front-side plasma and back-side plasma, the length of the back-side plasma becomes ~ 8 kpc, This means that a hotter plasma of large depth exists over the warm thin disk, because 4U 1820–303 lies 1 kpc below the Galactic disk.

3.3.2. Uniform plasma model of two absorbing component

For the second step, we assumed that two plasma components which exist in front of 4U 1820–303 contribute both the absorption and emission (model C2) as illustrated in figure 7. Note that this assumes that there is no emission from the bulge behind 4U 1820–303. It is not determined whether the two plasma components are separate, or mixed together with some filling factors, but we again set an upper limit for the length to be 7.6 kpc and a common velocity dispersion.

As with the previous model C1, we constructed two models with model sets of E2-mb + A4 (C2-1, C2-2) and E3-A' + A4 (C2-3, C2-4). The fitting results are shown in table 13. These values can be understood as follows;

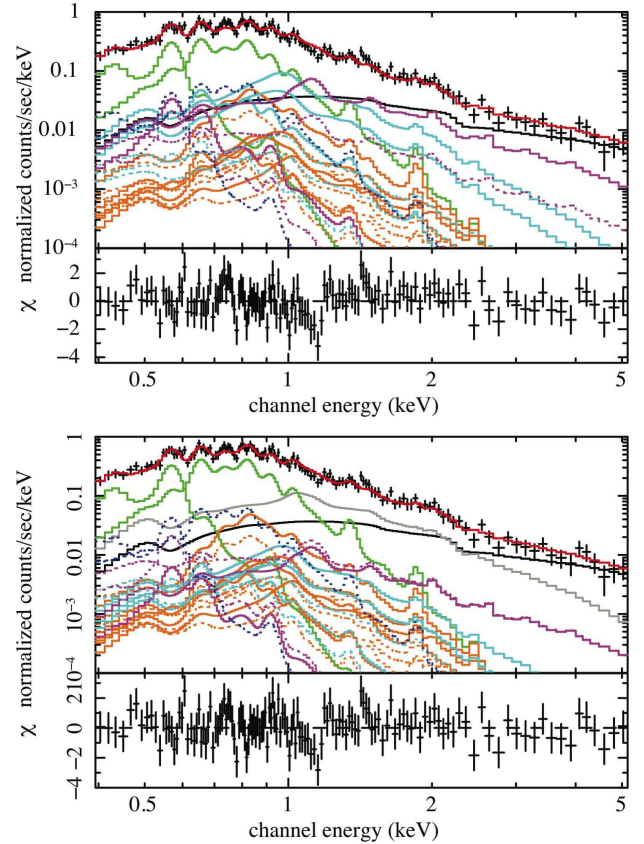


Fig. 5. Best-fitted model and spectra by model E2-mb and E3-A'. The dotted lines indicate foreground (unabsorbed) components and the solid lines indicate background (fully absorbed) components. hot ISM (green), CXB (black), SWCX+LHB, and Loop I (blue), stars except for M stars (orange), M stars (light blue), and RS CVns (magenta). Additional background continuum in E3 model is indicated by gray line.

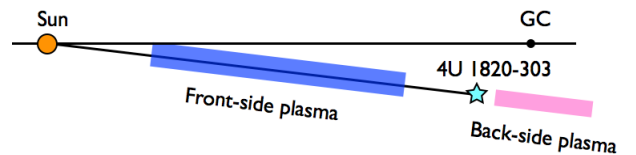


Fig. 6. Schematic view of the model C1.

First, two plasma components of temperatures $\sim 3.5 \times 10^6$ K and $\sim 1.0 \times 10^6$ K are required to reproduce the emission spectra. The ionization fraction and emissivity of each plasma is determined by their temperature, then the column density and the emission measure to reproduce the absorption spectrum are obtained. We confirm this flow and found that the emission measures obtained here are about half of those obtained in the emission analysis. This is caused by the slight temperature decrease of hotter plasma induced by this combined analysis.

With the model C2 results and the assumption of the Ne abundance of solar value, and the temperature dependence of the ionization fraction, the Ne X column density is at most $1 \times 10^{15} \text{ cm}^{-2}$. The upper limit of the column

Table 11. Fitting results of C1 model

Model		Front-Side plasma					Back-Side plasma		Stars Ratio ^b	Binaries Ratio ^c	Additional		χ^2
		$N_{\text{HHot}} (\text{cm}^{-2})$	Length (kpc)	$\log T$ (K)	Ne/O	v_b (km s^{-1})	$\log T$ (K)	Norm ^a			$\log T$ (K)	Norm	
C1-1	E2-mb	$19.71^{+0.09}_{-0.37}$	$7.60^{+0.00}_{-5.61}$	$6.22^{+0.05}_{-0.08}$	$6.583^{+0.055}_{-0.049}$	$15.5^{+5.1}_{-4.9}$	$7.00^{+1.90}_{-2.83}$	$4.66^{+1.56}_{-1.51}$	819.8
	A4	↑	...	↑	...	109^{+140}_{-29}	819.8
C1-2	E2-mb	$19.60^{+0.18}_{-0.22}$	$4.67^{+2.93}_{-2.91}$	$6.22^{+0.05}_{-0.06}$	$1.4^{+1.2}_{-0.8}$...	$6.588^{+0.047}_{-0.051}$	$15.3^{+5.2}_{-3.9}$	$6.67^{+1.98}_{-1.59}$	$4.86^{+1.48}_{-1.53}$	819.8
	A4	↑	...	↑	↑	126^{+164}_{-45}	819.8
C1-3	E3-A'	$19.68^{+0.16}_{-0.11}$	$5.88^{+1.72}_{-3.66}$	$6.20^{+0.05}_{-0.04}$	$6.574^{+0.041}_{-0.029}$	$22.0^{+3.0}_{-5.2}$	$7.254^{+0.085}_{-0.086}$	$37.7^{+5.2}_{-5.3}$	810.3
	A4	↑	...	↑	...	111^{+84}_{-34}	810.3
C1-4	E3-A'	$19.53^{+0.21}_{-0.19}$	$3.08^{+4.52}_{-1.81}$	$6.23^{+0.05}_{-0.05}$	$2.3^{+1.4}_{-1.1}$...	$6.592^{+0.040}_{-0.040}$	$18.9^{+5.1}_{-4.0}$	$7.265^{+0.089}_{-0.073}$	$37.1^{+5.0}_{-5.5}$	805.9
	A4	↑	...	↑	↑	139^{+195}_{-55}	805.9

Note: All the parameters not written the table is fixed to the simulation based values.

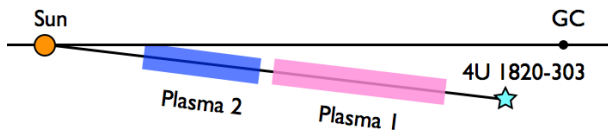
^aEmission Measure $10^{-3} \int n_e n_p dl$: in unit of $\text{cm}^{-6} \text{pc}$

^bNormalization of background M type star is set to be free

^cRatio of the normalization of the background stars or binaries to the simulation based value

Table 12. Physical properties obtained by the model C1-4

Model	Component	Length (kpc)	Density (10^{-3}cm^{-3})	Temperature (10^6K)	Pressure ($10^3 \text{cm}^{-3} \text{K}$)
C1-4	Front-Side plasma	$3.08^{+4.52}_{-1.81}$	$3.6^{+10.4}_{-2.6}$	$1.7^{+0.2}_{-0.2}$	$6.0^{+20.6}_{-4.6}$
	Back-Side plasma	1	$4.3^{+0.6}_{-0.4}$	$3.9^{+0.4}_{-0.3}$	$16.8^{+4.2}_{-2.9}$
		2	$3.1^{+0.6}_{-0.4}$	↑	$12.1^{+3.7}_{-2.5}$
		10	$1.4^{+0.2}_{-0.2}$	↑	$5.1^{+1.3}_{-1.2}$

**Fig. 7.** Schematic view of the model C2.

density of Ne X from that of EW in the absorption spectrum in table 2 is $\log N_{\text{NeX}} = 15.4$, and is consistent with this upper limit.

We summarized the induced physical properties of the plasma in table 14. The length of the hotter plasma is almost on the upper limit. While the cooler component has very short length $< 0.7 \text{ kpc}$ and the pressure is higher than that of the hotter by a factor of ~ 7 . This assumption gives a scheme of a thin warm and a thick hot disk halo model.

3.4. Uncertainty due to the model systematics

In the absorption analysis, the energy resolution of the detectors ($\sim 0.05 \text{ \AA}$) corresponds to $v_b \sim 400 \text{ km s}^{-1}$ and is not enough to determine the v_b of the plasma only with the line shapes. The lower limit of v_b can be determined from thermal limits. Thus, to determine the velocity dispersion, we used the ratio of the absorption depth of O VII K_α and O VII K_β instead and assumed that the O VIII, Ne IX and Ne X originate from the same plasma, and linked the velocity dispersion of all lines. As v_b and column density are coupled and if the plasma has a temperature gradient and local structure, this assumption causes systematic errors,

but it effects little in the temperature of the ISM as shown by Hagihara et al. (2010).

In table 15 we summarize the systematic errors of the background and foreground models and their effect on the best fit values of the hot ISM parameters. The obtained hot ISM parameters are all within 90 % statistical error and cause no change to our results and conclusions.

In addition to the systematic errors mentioned above, we have to consider systematics caused by the combined analysis itself. Figure 8 shows contours of the temperatures of the hot ISM derived from emission analysis (E3-A') and combined analysis (C1-4, C2-4). As shown in figure 8, contours only overlap partially and those from combined analysis are shifted to each direction. The best fitted χ^2/dof value of C1-4 model is worse than those of the other models. These shifts would be caused by modeling a multi-temperature plasma with two temperature plasmas. To check the contribution of the uncertainty of the star and unknown component, we fixed the parameters of the unknown component to the best fit value of E3-A' model (table 9) and performed a combined analysis with the C1-4 and C2-4 models. The results are consistent with those of C1-4 and C2-4 model. These two models (C1-4, C2-4) are representative of the other combined analysis models and we concluded the systematics originate in the combined analysis. Using these contours, the temperature range of the two plasmas are determined as $2.8 - 4.3 \times 10^6 \text{ K}$ and $0.68 - 1.9 \times 10^6 \text{ K}$.

We also checked the self-absorption effect of the emission lines with the obtained column density and veloc-

Table 13. Fitting results with C2 model

Model		Uniform hot plasma 1					Uniform hot plasma 2			Stars Ratio ^a	Binaries Ratio ^b	Addition log T (K)
		$N_{\text{H}_{\text{Hot}}}$ (cm^{-2})	Length (kpc)	log T (K)	Ne/O	v_b (km s^{-1})	$N_{\text{H}_{\text{Hot}}}$ (cm^{-2})	Length (kpc)	log T (K)			
C2-1	E2-mb	$19.55^{+0.04}_{-0.24}$	$7.6^{+0.0}_{-5.2}$	$6.48^{+0.04}_{-0.04}$	$19.26^{+0.33}_{-0.32}$	$0.17^{+0.66}_{-0.15}$	$5.99^{+0.07}_{-0.15}$	$7.58^{+1.92}_{-1.81}$	$4.73^{+1.47}_{-1.46}$...
	A4	↑	...	↑	...	139^{+286}_{-44}	↑	...	↑
C2-2	E2-mb	$19.55^{+0.04}_{-0.22}$	$7.6^{+0.0}_{-5.1}$	$6.48^{+0.04}_{-0.04}$	$0.9^{+0.4}_{-0.4}$...	$19.26^{+0.34}_{-0.31}$	$0.18^{+0.67}_{-0.16}$	$5.99^{+0.07}_{-0.15}$	$7.85^{+2.01}_{-2.09}$	$4.56^{+1.61}_{-1.62}$...
	A4	↑	...	↑	...	140^{+282}_{-44}	↑	...	↑
C2-3	E3-A'	$19.57^{+0.03}_{-0.22}$	$7.5^{+0.1}_{-4.9}$	$6.51^{+0.02}_{-0.03}$	$19.22^{+0.37}_{-0.25}$	$0.2^{+0.7}_{-0.1}$	$6.01^{+0.07}_{-0.10}$	$7.247^{+0.069}_{-0.094}$
	A4	↑	...	↑	...	156^{+269}_{-64}	↑	...	↑
C2-4	E3-A'	$19.52^{+0.16}_{-0.21}$	$5.9^{+1.7}_{-3.7}$	$6.50^{+0.03}_{-0.04}$	$1.4^{+0.4}_{-0.3}$...	$19.19^{+0.33}_{-0.25}$	$0.13^{+0.56}_{-0.11}$	$6.00^{+0.07}_{-0.11}$	$7.270^{+0.082}_{-0.069}$
	A4	↑	...	↑	...	169^{+273}_{-76}	↑	...	↑

Note: All the parameters not written the table is fixed to the simulation based values.

^aNormalization of background M type star is set to be free

^bRatio of the normalization of the background stars or binaries to the simulation based value

^cEmission Measure $10^{-3} \int n_e n_p dl$: in unit of $\text{cm}^{-6} \text{pc}$

Table 14. Physical properties obtained by model C2-4

Model	Component	Length (kpc)	Density (10^{-3}cm^{-3})	Temperature (10^6K)	Pressure ($10^3 \text{cm}^{-3} \text{K}$)
C2-4	Plasma 1	$5.9^{+1.7}_{-3.7}$	$1.8^{+5.2}_{-0.9}$	$3.2^{+0.2}_{-0.3}$	$5.7^{+18.1}_{-3.2}$
	Plasma 2	$0.13^{+0.56}_{-0.11}$	$38.6^{+497.3}_{-34.5}$	$1.0^{+0.2}_{-0.2}$	$38.6^{+591.0}_{-35.4}$

Table 15. Estimated systematic errors of the models and their effect on the best fit values of the hot ISM parameters (all the parameters are within statistical error).

Component	Systematic Error	Affection to the best fit values of the Hot ISM			
		Cool ($T < 1.3 \times 10^6 \text{K}$)		Hot ($T > 2.5 \times 10^6 \text{K}$)	
		Temperature	Normalization	Temperature	Normalization
Foreground stars	+20%	< 1%(+)	-3%	< 1%(-)	< 1%(-)
	-20%	< 1%(-)	+3%	< 1%(+)	< 1%(+)
Background stars	+50%	< 1%(-)	+2%	< 1%(-)	-2%
	-50%	< 1%(+)	-2%	< 1%(+)	+2%
CXB	+30%	< 1%(+)	$\pm 3\%$	< 1%(-)	$\pm 1\%$
	-30%	< 1%(-)	$\pm 3\%$	< 1%(+)	$\pm 1\%$
LHB+SWCX	+75%	< 1%(+)	-15%	< 1%(+)	< 1%(±)
	-100%	< 1%(-)	+18%	< 1%(+)	< 1%(±)
Loop I	+50%	< 1%(+)	-3%	< 1%(-)	-10%
	-50%	< 1%(-)	+4%	< 1%(+)	+10%

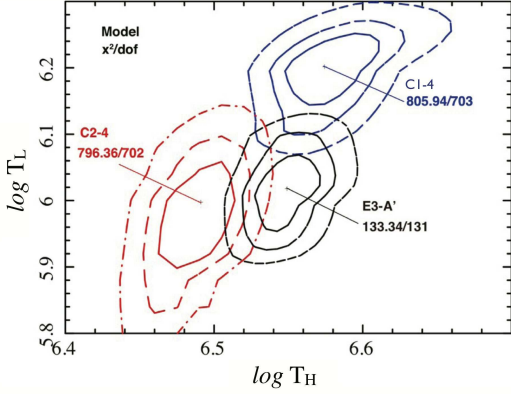


Fig. 8. 68%, 90%, and 99% confidence contours of the temperature of hot ISM for two parameters. Black, red and blue lines indicate the results of E3-A' model, C1-4 model and C2-4 model respectively. The best fitted χ^2/dof values are indicated.

ity dispersion of ions. When the column density O VII is 10^{16}cm^{-2} and the minimum velocity dispersion $v_b = 200 \text{ km s}^{-1}$, the opacity τ at the center of the resonance line is ~ 1.1 , which is evaluated in the same way as Futamoto et al. (2004). The reduction due to the self-absorption for the resonance line is about 30% after integrating over the emission line profile. Note that we measured all resonance, inter-combination, and forbidden lines as O VII line, with the energy resolution of the Suzaku XIS. As the oscillator strength of the forbidden line is very small, the apparent reduction is diluted to be half as small as 15%. Also we neglected the effect of scattered-in photons from outside the line of sight. The τ at the O VIII line center is less than the unity with $b = 200 \text{ km s}^{-1}$ and $N_{\text{O VIII}} = 10^{16} \text{ cm}^{-2}$, and the total reduction is less than 20% without considering the $\text{O VII K}\beta$ line. These effects will systematically reduce the emission line intensity, but we neglect the effect in this paper because the correction is as much as the systematic and statistical errors. When we obtain the better energy resolution for the diffuse emission, we will be able to evaluate by the ratio between the resonance and forbidden lines.

4. Discussion

In this paper, we analyzed emission and absorption spectra toward the Galactic bulge region, and found that there are at least two models to explain the emission and absorption data in this direction. We summarized the results in table 16. Only the emission measures are obtained for the back-side component, because there are no absorption data. As we simplified the models as much as possible, we will discuss the hot plasma within our Galaxy by possible extension from current simple models and by comparing the previous results at high latitude.

4.1. Extension of the current simplest geometry

First, we took notice of the length of the front component. It is not likely that such a fully filled component is confined only in a sight line, and this implies that these components fill and prevail throughout the disk. Thus, we consider that such long extended plasma is a part of the hot ISM disk. Except for Plasma 2 in C2 model, the error range includes the upper limit determined by the geometry, which is the distance of 7.6 kpc toward 4U1820–303. It is not reasonable that the boundary of the two plasmas coincide at 4U1820–303. It is useful to consider what happens when a plasma of the same temperature exists beyond 7.6 kpc as in figure 9. Additional plasma at the backside of 4U 1820–303, which does not contribute to the absorption, makes the emission measure of the original plasma decrease to maintain the emission intensity, while the column density is constant. The length becomes longer and the density becomes smaller assuming additional distant plasma. If the density of absorbing plasma is reduced by a factor of $1/c$, and the length is increased by the same factor c , the column density is kept as the same and the emission measure is reduced by $1/c$. Thus if there is emitting plasma behind the target with density n/c and length of $c(c-1)$ times the original one, the emission measure is recovered. It is easily written with the density n , the length L and a reduction factor c ,

$$CD = n/c \times cL = nL \quad (1)$$

$$EM = (n/c)^2 \times cL + (n/c)^2 \times c(c-1)L = n^2L \quad (2)$$

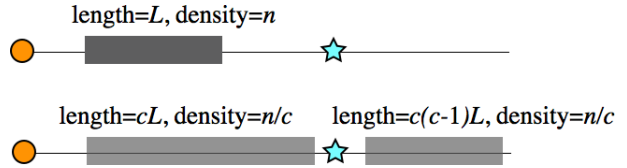


Fig. 9. Schematic view of the extended plasma model beyond 4U1820–303.

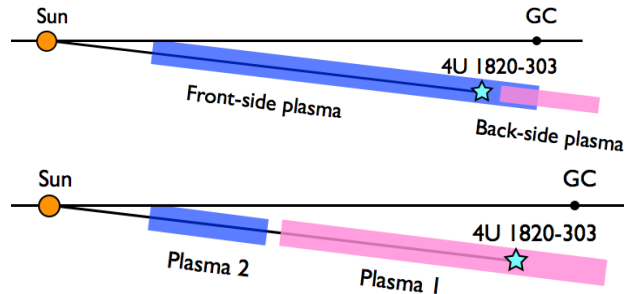


Fig. 10. Elongated models correspond to case C1 and C2 (C1-B and C2-B)

Both C1 and C2 models can be extrapolated like figure 10 as case C1-B and C2-B.

4.2. Comparison with the exponential disk observed at the high latitude

The C1 model implies a thin warm disk with a length of 3.1 kpc in the front and a hot plasma at the back, toward the bulge region. The hot plasma is possible to associate with the bulge, or to be a hot thick disk above the warm disk. We will compare the properties of the warm disk with the exponential disk model obtained by the combined analysis with absorption to extragalactic objects; PKS2155–304 (Hagihara et al. 2010) and LMC X-3 (Yao et al. 2009). In the extreme case, we can assume that the warm plasma has an extent of 7.6 kpc which corresponds to $c = 7.6/3.1 = 2.5$ in the above equations 1 and 2. The total length and the total column density are calculated as $(cL + c(c-1)L) = c^2L = 19.4$ kpc and $nL + (c-1)nL = cnL = 10^{19.93} \text{ cm}^{-2}$. The thickness of the disk is $19.4 \times \sin(b_{4U}) = 2.7$ kpc, where $b_{4U} = -7.9^\circ$ is the Galactic latitude of 4U 1820–303. This is comparable to that of the exponential disk. The column density is also comparable to that found for PKS2155–304 considering the difference of the Galactic latitude, as $10^{19.93} \times \sin(b_{4U})/\sin(b_{\text{PKS}}) = 10^{19.17} \text{ cm}^{-2}$, where $b_{\text{PKS}} = -52.2^\circ$ is the Galactic latitude of PKS 2155–304. This value is consistent with the column density for the PKS 2155–304 direction, $\log N_{\text{H}} = 10.10^{+0.08}_{-0.07}$ obtained by an exponential disk model (Hagihara et al. 2010). Thus the front plasma of C1 model corresponds to the exponential disk.

To confirm this similarity, we applied an exponential disk model with parameters, which represent well both the emission and absorption spectra of PKS 2155–304 (Hagihara et al. 2010). The exponential model well matched the absorption spectrum, but failed for the emission spectrum due to the residuals below 1 keV. If we add components which only contribute to the emission like C1 model, the fit returns a $\chi^2 = 809.8/706$ with two thermal component with $\log T = 6.597^{+0.046}_{-0.044}$ and $6.023^{+0.251}_{-0.183}$ with a stellar contribution the same as in E3-A’.

The hot plasma at the backside was not observed at high latitude with LMC X-3 and PKS2155–304 (Yao et al. 2009; Hagihara et al. 2010), but was detected in observations toward other bulge regions (Almy et al. 2000). The temperature and estimated electron density assuming the size of 10 kpc is consistent with those by the RASS image model by Snowden et al. (1997). These support the idea that the back-side plasma is a hot plasma associated with the bulge region. The location, size, and pressure are, however, not determined by current observations, and the relation between the disk and the bulge is hard to be considered.

The C2 model implies a thin warm and thick hot disk halo model. Such a thin disk has not been observed by previous studies, and its pressure is as high as $4 \times 10^4 \text{ cm}^{-3} \text{ K}$, and almost twice of the typical value at the midplane estimated by Cox (2005) with thermal and non-thermal (Cosmic rays and magnetic field) components. The pressure of the warm plasma is also not balanced by a factor of 6. In addition, this simple C2 model assumes that the

hot ISM is spatially limited in front of 4U1820-303 and no plasma in the bulge region. If the hotter plasma can be extended beyond 4U1820–303 like C2-B in figure 10, the pressure will decrease in proportional to the density. We thus need some mechanism to confine the warm $T \sim 10^6$ K plasma close to the Galactic disk.

5. Conclusion

We have analyzed high resolution X-ray absorption/emission data observed by Chandra and Suzaku to determine the physical properties of the hot ISM toward the galactic bulge (4U 1820–303) direction with an estimate for the contribution from normal stars in the soft X-ray band.

A two component plasma model can reproduce the absorption and emission spectra. One model assumes that only one component contributes to the absorption in front of 4U 1820–303. The temperature, column density and length of the front plasma are determined as $1.7^{+0.2}_{-0.2} \times 10^6$ K, $3.4^{+2.1}_{-1.2} \times 10^{19} \text{ cm}^{-2}$ and $3.1^{+4.5}_{-1.8}$ kpc. The temperature and emission measure of the back-side plasma are determined as $3.9^{+0.4}_{-0.3} \times 10^6$ K and $18.9^{+5.1}_{-4.0} \text{ cm}^{-6} \text{ pc}$. This model is consistent with a scheme with a hot X-ray bulge and an exponential disk model obtained from extragalactic source observations. If there are two plasma components contributing to the absorption, a thin warm plasma disk with temperature of $1.0^{+0.2}_{-0.2} \times 10^6$ K and a length of $0.13^{+0.56}_{-0.11}$ kpc is confined to the Galactic disk, and it is not pressure-balanced with a hot thick disk with temperature of $3.2^{+0.2}_{-0.3} \times 10^6$ K.

Part of this work was financially supported by Grant-in-Aid for Scientific Research (Kakenhi) by MEXT, No. 20340041, 20340068, and 20840051. TH appreciates support from the JSPS research fellowship and the Global COE Program “the Physical Sciences Frontier”, MEXT, Japan.

References

- Almy, R.C., McCammon, D., Digel, S.W., Nronfman, & L., May, J. 2000, ApJ, 545,290
- Anders, E., & Grevesse, N. 1989, Geochim. Cosmochim. Acta, 53, 197
- Cox, D. P. 2005, ARA&A, 43,337
- Egger, R.J., & Aschenbach, B. 1995, A&A, 294, L25
- Ferriere, K. 1998, ApJ, 503, 700
- Fujimoto, R., et al. 2007, PASJ, 59, S133
- Futamoto, K., Mitsuda, K., Takei, Y., Fujimoto, R., & Yamasaki, N. Y. 2004, ApJ, 605, 793
- Girardi, L., Groenewegen, M. A. T., Hatziminaoglou, E., & da Costa, L. 2005, A&A, 436, 895
- Hagihara, T., Yao, Y., Yamasaki, N. Y., Mitsuda, K., Wang, Q. D., Takei, Y. Yoshino, T. & McCammon, D. 2010, PASJ, 62, 723
- Hasinger, G., Burg, R., Giacconi, R., Hartner, G., Schmidt, M., Trumper, J., & Zamorani, G. 1993, A&A, 275, 1
- Ishisaki, Y., et al. 2007, PASJ, 59, S113

Table 16. Results of the analysis of the galactic bulge region.

Model	Component	Front-Side			Back-Side	
		T (10^6K)	$\log N_{\text{HHot}}$ (cm^{-2})	Length (kpc)	T (10^6K)	EM ($10^{-3}\text{cm}^{-6}\text{pc}$)
C1	Front-Side Plasma	1.7 ± 0.2	19.53 ± 0.2	$3.1^{+4.5}_{-1.8}$
	Back-Side Plasma	$3.9^{+0.4}_{-0.3}$	$18.9^{+5.1}_{-4.0}$
C2	Plasma 1	$3.2^{+0.2}_{-0.3}$	$19.52^{+0.16}_{-0.21}$	$5.9^{+1.7}_{-3.7}$
	Plasma 2	1.0 ± 0.2	$19.19^{+0.33}_{-0.25}$	$0.13^{+0.56}_{-0.11}$

- Kalberla, P. M. W., Burton, W. B., Hartmann, D., Arnal, E. M., Bajaja, E., Morras, R., & Pöppel, W. G. L. 2005, *A&A*, 440, 775
- Koyama, K., et al. 2007, *PASJ*, 59, 23
- Kuntz, K. D., & Snowden, S. L., 2001, *ApJ*, 554, 684
- Kuulkers, E., den Hartog, P. R., in't Zand, J. J. M., Verbunt, F. W. M. Harris, W. E. & Cocchi, M. 2003, *A&A*, 399, 633
- López-Santiago, J., Micela, G., Sciortino, S. K., Favata, F., Caccianiga, A., Della Ceca, R., Severgnini, & P., Braitto, V. 2007, *A&A*, 463, 165
- Masui, K., Mitsuda, K., Yamasaki, N. Y., Takei, Y., Kimura, S., Yoshino, T., & McCammon, D., 2009, *PASJ*, 61, 115
- Mitsuda, K., et al. 2007, *PASJ*, 59, S1
- Nicastro, F., et al. 2005, *Nature*, 433, 495
- Sciortino, S., Maggio, A., Favata, F., & Orlando, S. 1999, *Å*, 342, 502
- Skrutskie, M. F., et al. 2006, *AJ*, 131, 1163
- Smith, R. K., et al. 2007, *PASJ*, 59, S141
- Snowden, S.L. et al. 1993, *ApJ*, 404, 403
- Snowden, S. L., Egger, R., Freyberg, M. J., McCammon, D., Plucinsky, P. P., Sanders, W. T., Schmitt, J. H. M. M., Truemper, J., & Voges, W. 1997, *ApJ*, 485, 125
- Ottmann, R., & Schmitt, J. H. M. M. 1992, *A&A*, 256, 421
- Park, S., Finley, J.P., Snowden, S.L., & Dame, T.M. 1997, *ApJL*, 476, L77
- Rocks, L.E. 2009, PhD thesis, University of Wisconsin
- Tawa, N. et al. 2008, *PASJ*, 60, S22
- Udalski, A., Szymanski, M., Kubiak, M., Pietrzynski, G., Wozniak, P., & Zebrun, K. 1997, *Acta Astronomica*, 47, 431
- van den Besselaar, E. J. M., Raassen, A. J. J., Mewe, R., van der Meer, R. L. J., Güdel, M., & Audard, M. 2003, *A&A*, 411, 587
- Vanhollebeke, E., Groenewegen, M. A. T., & Girardi, L. 2009, *A&A*, 498, 95
- Yao, Y., & Wang, Q. D. 2006 *ApJ*, 641, 930
- Yao, Y., Wang, Q. D., Hagihara, T., Mitsuda, K., McCammon, D., & Yamasaki, N. Y. 2009, *ApJ*, 690, 143
- Yoshino, T., et al. 2009, *PASJ*, 61, 805